Low Sensitivity of Acoustic Breathing Mode Frequency in Co Nanocrystals upon Change in Nanocrystallinity

Dario Polli,[†] Isabelle Lisiecki,[‡,§] Hervé Portalès,[‡,§] Giulio Cerullo,[†] and Marie-Paule Pileni[‡,§,*]

[†]IFN-CNR, Dipartimento di Fisica, Politecnico di Milano, P.za L. da Vinci 32, 20133 Milano, Italy, [‡]Université Pierre et Marie Curie, UMR 7070, LM2N, 4 place Jussieu 75005 Paris, France, and [§]Centre National de la Recherche Scientifique, UMR 7070, LM2N, 4 place Jussieu 75005 Paris, France

ABSTRACT Cobalt nanocrystals (NCs) with narrow size distribution and polycrystalline structure in their native form are synthesized in reverse micelles. After annealing at 350 °C, these NCs are transformed into single crystalline phase with hexagonal close-packed structure. The vibrational dynamics of NCs differing by their nanocrystallinity is studied by femtosecond pump−probe spectroscopy. By recording the differential reflectivity signal in the native and annealed Co NCs, the frequency of their fundamental breathing acoustic mode can be measured in the time domain. A small decrease of the breathing mode frequency is observed in single crystalline Co NCs compared to that measured in polycrystals, indicating low sensitivity of their fundamental radial mode upon change in crystallinity. This result is in agreement with predictions from calculations using the resonant ultrasound approach.

KEYWORDS: time-resolved pump−probe spectroscopy · acoustic vibrations · breathing mode · anisotropic elasticity · polycrystals · single crystals

During the past few years, metallic nanometer-sized particles have attracted considerable interest primarily motivated by the capability of tailoring their physical properties simply through control of their size, shape, and environment. In particular, extensive experimental and theoretical studies have been devoted to the acoustic vibrations of these nanoparticles. As a consequence of the reduction in the particle size, the acoustic phonons become discrete and the confined vibrational modes, which typically lie in the terahertz range, have frequencies inversely proportional to the particle diameter. To observe such low-frequency acoustic modes, frequency-domain methods such as Raman scattering spectroscopy[1−3] and time-domain approaches such as femtosecond pump−probe spectroscopy[4−6] have been successfully used for various metal nanoparticles.

Different selection rules apply to the vibrational modes detected by frequency- or time-domain techniques. For instance, the fundamental radial (breathing) mode is the main contribution detected in the dynamical response of quasispherical metal nanocrystals (NCs) measured by pump−probe experiments.[7] At variance, Raman scattering of metal NCs is dominated by their quadrupolar modes[3] while the breathing mode and higher order radial modes[7−10] are only observable by this technique from samples with narrow size distribution.

Until recently, most of the acoustic vibrational frequencies measured in metal NCs were successfully interpreted by modeling the vibrations of these particles as those of an elastically isotropic homogeneous sphere.[11] Owing to significant advances in particles synthesis, better control of their nanocrystallinity has been achieved, making it possible to produce batches of NCs with a large fraction of single crystalline ones.[12] Recent low-frequency Raman experiments performed on Au NCs mainly composed of single crystal phase showed their Raman spectra to be dramatically affected by the highly anisotropic elasticity of these NCs through the splitting of their quadrupolar mode.[13−15] Besides, comparing the time-resolved responses of Ag NCs with either polycrystalline or single crystalline structures, the frequency of the breathing mode was observed to sensitively depend on crystallinity, with a ~15% increase in frequency observed for the single crystalline particles.[12] Calculations using either a resonant ultrasound (RUS) approach[16] or a finite-element analysis method,[17] while correctly reproducing the dependence on nanocrystallinity of the quadrupolar mode observed in the Raman spectra of Au NCs, predict however a negligible change in the breathing mode frequency for Ag NCs, at variance with the single experimental observation of such an effect.[12] From the results reported to date, the actual effect of nanocrystallinity on the breathing mode frequency of metal NCs still remains an open question.
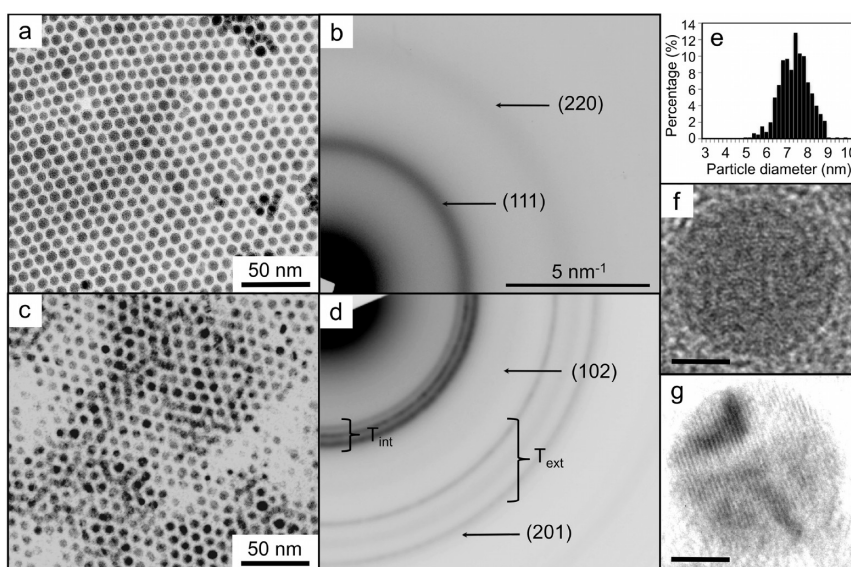
Figure 1. (a) TEM image and (b) ED pattern of native Co NCs compared to those obtained after their annealing at 350 °C (c, d). (e) Size distribution histogram of the native NCs determined over 500 entities. (f, g) HRTEM images showing a native highly disordered polycrystalline Co NC and a single-crystalline Co NC with hcp structure, respectively. The scale bars in the images f and g correspond to 2 nm.

In the attempt to mitigate this controversy, the present work is devoted to study in parallel the dynamical responses of Co NCs with either polycrystalline structure or hexagonal close-packed (hcp) single crystal structure. Femtosecond transient reflectivity measurements are used here to determine the frequency of the breathing mode in both types of nanocrystals. A comparison of the measured frequencies with calculated ones is also presented to support the assignment of the observed oscillations to the fundamental breathing acoustic mode of these nanocrystals.

RESULTS AND DISCUSSION

Structural Characterization of Co NCs. To characterize the Co NCs in both their native and annealed states, we first investigate by transmission electron microscopy (TEM) their two-dimensional (2D) assemblies. Figure 1a shows that native Co NCs long-range self-organize in a 2D hexagonal network. Their electron diffraction (ED) pattern (Figure 1b) is characterized by two diffuse rings related to lattice spacings of 2.04 ± 0.04 Å and 1.20 ± 0.04 Å that are indexed as the (111) and (220) reflections of face-centered cubic Co lattices, respectively. The size distribution of these nanocrystals (Figure 1e), determined by TEM analysis, is performed over a population of *ca*. 500 nanocrystals. The mean NC diameter is 7.3 ± 0.2 nm with 10% as the size distribution. By high-resolution transmission electron microscopy (HRTEM), one observes that these NCs are composed of a few crystalline domains, defined as small-domains particle, (Figure 1f) whose typical size does not exceed 1 nm.[18] After annealing at 350 °C, all the hcp Co phase reflections up to the second order are observed (Figure 1d). Eight thin rings characterized by

0.217, 0.203, 0.192, 0.145, 0.125, 0.116, 0.106, and 0.104 nm distances correspond to the (100), (002), (101), (102), (110), (103), (112), and (201) planes of the hcp Co phase, respectively. As illustrated in Figure 1g, HRTEM observations indicate that the annealed NCs are mostly single crystalline with regular lattice planes characterized by the 1.91 Å spacing. This structural study clearly evidences that the annealing treatment of Co NCs favors their crystallographic transition from a highly disordered polycrystalline structure to the hcp Co single-crystalline one.

To further confirm both the annealing induced crystallographic transition of Co NCs and their high thermal stability, we investigated the low-field magnetic behavior of their three-dimensional (3D) assemblies. The samples used here are the same as those for the time-resolved experiments described below. These assemblies look like an inhomogeneous film whose topology has been checked to be quasi-unaffected by the annealing process.[19] Figure 2 panels a and b show the normalized-field cooled (FC) and zero-field cooled (ZFC) magnetization *versus* temperature curves measured before and after annealing, respectively. The native sample is characterized by a blocking temperature T_B of around 100 K indicative of poorly crystallized 7.3 nm Co NCs with strong particle interactions.[19] Annealing the sample at 350 °C induces a drastic increase in T_B, which reaches *ca*. 280 K (Figure 2b). This behavior is explained by the crystallographic transition of the Co NCs from a small-domains particle to the single-crystalline hcp structure. This leads to an increase in the magnetic anisotropy of the Co NCs, which in turn induces an increase in the energy barriers and hence in T_B.[19] As shown in Figure 2c, the ZFC curves
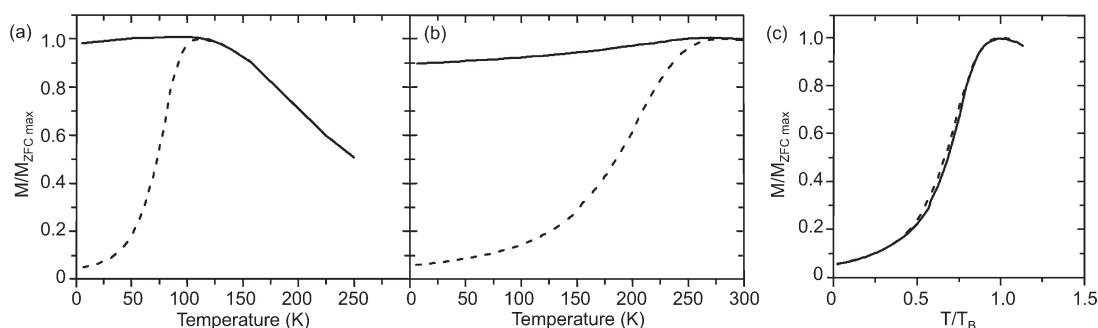
Figure 2. Normalized FC (continuous line) and ZFC (dotted line) magnetization *versus* temperature curves of 7.3 nm Co NCs measured (a) before annealing, that is, in native nanocrystals, and (b) after annealing at 350 °C. (c) Comparison of the ZFC curves of the native and annealed Co NCs after normalizing both curves to the blocking temperature T_B.
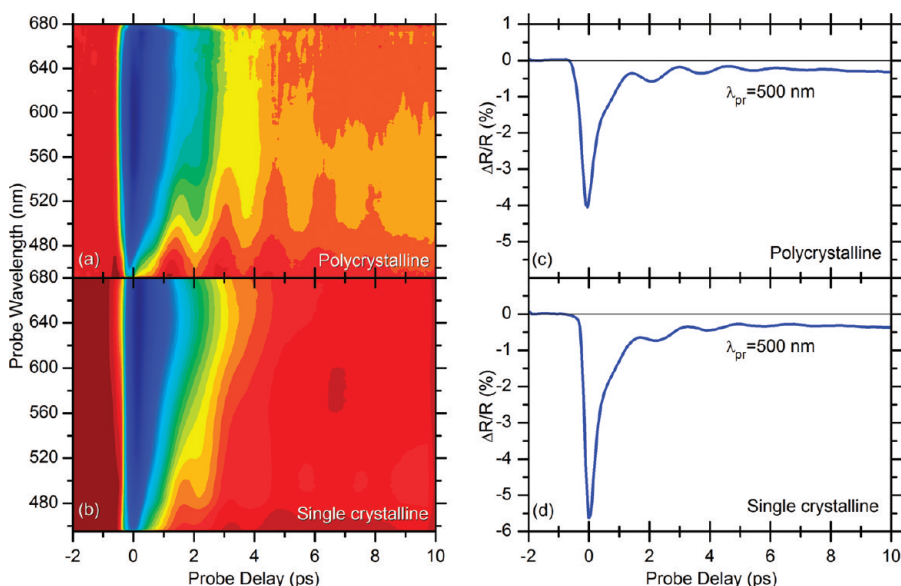

Figure 3. 2D map showing the $\Delta R/R$ signal amplitude as a function of both probe delay and wavelength for (a) polycrystalline and (b) single crystalline 7.3 nm Co NCs deposited on HOPG substrate. $\Delta R/R$ time traces extracted from the 2D map by horizontal cuts at the probe wavelength $\lambda_{pr} = 500$ nm for (c) polycrystalline and (d) single crystalline Co NCs.

normalized to T_B of Co NCs in the native and annealed states are perfectly superimposed. This indicates that neither aggregation nor coalescence have occurred, which would lead to an increase in the nanocrystal size distribution, that is, an increase in the distribution of barrier energies and a broadening of the ZFC peak.[19] In addition, the similarity of the magnetic behavior before and after annealing allows us to discount any effect of size during the annealing process of fcc supracrystals.[19,20] Indeed, T_B is very sensitive to the nanocrystal diameter as it is found that changing this latter by 1 nm results in a change of T_B by 43 K. The absence of 8 K peak[21] on the ZFC curve confirms that Co NCs are stable against oxygen both in their native and annealed states, in the detectable range. All these results allow us to conclude that the conversion to the single-crystalline hcp structure is complete after annealing at 350 °C. These magnetic studies performed on 3D fcc supracrystals confirm the structural studies made on Co nanocrystals monolayers,[20] which indicate that the

average diameter of the annealed NCs remains quasi-unchanged compared to that of the native nanocrystals.

The high stability of the native and annealed Co NCs against coalescence and oxidation is likely to originate from the dodecanoic acid molecules that are chemically bound to their surface. Typically used as coating agent, these molecules probably play a key role in both maintaining the integrity of the coated NCs and preventing their oxidation. Interestingly, this behavior makes it possible to compare the properties of native and annealed Co NCs with the same size and environment but differing by their nanocrystallinity. In this regard and due to their respective structural characteristics, the native and annealed Co NCs will be referred to as poly- and single crystalline NCs, respectively, in the following part of the paper dedicated to their vibrational study performed by femtosecond pump—probe spectroscopy.
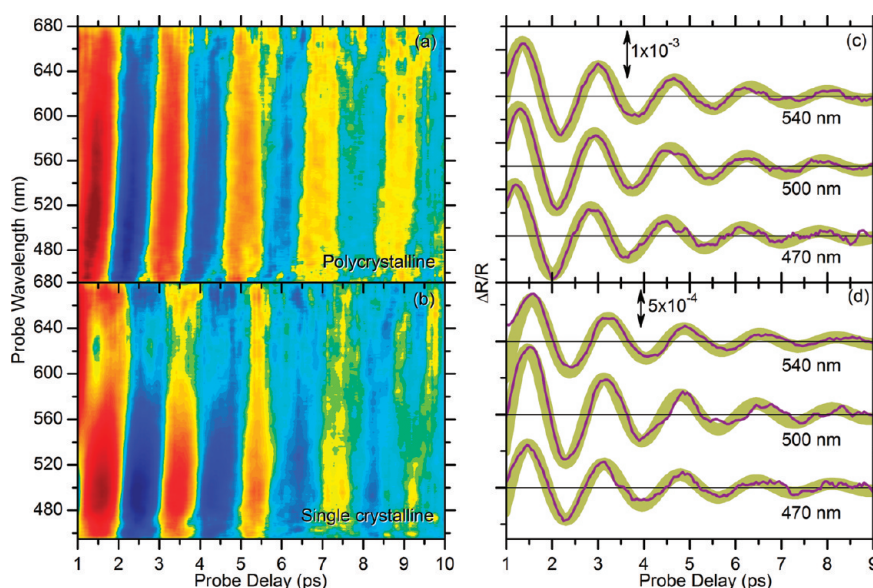
Figure 4. 2D map showing the variation of the $\Delta R/R$ signal amplitude as a function of both probe delay and wavelength for (a) polycrystalline and (b) single crystalline Co NCs after subtracting the slowly varying background signal. Oscillating component of the $\Delta R/R$ signal extracted from the 2D map of (c) polycrystalline and (d) single crystalline Co NCs at three different selected probe wavelengths, i.e., 470, 500, and 540 nm. Green thick curves are the best fist to the dynamics curves using the function defined by eq 1. The traces plotted in (c) and (d) are vertically shifted for clarity.

Femtosecond Pump—Probe Measurements. We recorded the time-resolved differential reflectivity ($\Delta R/R$) signal in polycrystalline and single crystalline Co NCs deposited on highly ordered pyrolytic graphite (HOPG) substrates by using the femtosecond pump—probe technique described in the Experimental Methods section. Figure 3 panels a and b show the two-dimensional (2D) $\Delta R/R$ maps as a function of probe delay and wavelength. From these maps, a negative reflectivity change ($\Delta R/R < 0$) is first observed throughout the probe wavelength range. The decrease in the reflectivity of the sample is originating from the pump-induced heating of the electron distribution within the Co NCs. By horizontal cuts, one can extract from these 2D maps the dynamical curves describing the time-dependent $\Delta R/R$ signal at chosen probe wavelengths, λ_{pr}. The results for poly- and single crystalline phase, at $\lambda_{pr} = 500$ nm, are plotted in Figure 3 panels c and d, respectively. The $\Delta R/R$ signal rises within ~150 fs, which corresponds to the instrumental temporal resolution, and decays within less than 2 ps to form a long-lived oscillating plateau that lasts a few picoseconds. The fast decay is attributed to electron—phonon interactions.[22] The oscillating pattern superimposed on the $\Delta R/R$ signal reveals the modulation of the reflectivity signal caused by coherent acoustic vibrations of the Co NCs launched by the ultrashort pump pulse. No such oscillations are observed when measuring the $\Delta R/R$ signal from a bare HOPG plate as it was confirmed by separate measurements not shown here. No major differences are observed between the two samples. These oscillations recorded across several

microscopic areas and on several samples are nicely reproducible (see Supporting Information).

To better distinguish the oscillating component in the $\Delta R/R$ signal and facilitate its study, the slowly varying background signal was subtracted from the measured traces after fitting the data with biexponential decay curves with time constants in the $1-100$ ps range. The resulting maps, in which the oscillatory component of the residual signal is solely represented, are shown in Figure 4 panels a and b for the polycrystalline and single crystalline Co NCs, respectively. Looking at these maps now allows for the clear observation of the oscillating pattern for both samples at each probe wavelength. The oscillations are visible for about five periods and their damping time is consistent with the low NC size distribution (10%). The presence in the two maps of similar parallel bands with regular thicknesses, which successively appears in blue and red/yellow colors, indicates that the periodicity of the oscillations is not significantly affected either by the probe wavelength or by a change in the particle nanocrystallinity.

To extract quantitative information of the acoustic vibrations of the Co NCs, we plot (Figure4c,d) the time traces of the oscillating component of the $\Delta R/R$ signal measured at three selected probe wavelengths as extracted from the 2D maps displayed in Figure 4a,b. All the traces have been fitted (see gray thick lines in Figure 4c,d) with a damped sinusoidal function of the form

$$f(t) = A \exp\left(-\frac{t}{\tau_d}\right)\sin(2\pi\nu t + \phi) \qquad (1)$$

where A, ϕ, τ_d, and ν are the initial amplitude, phase, the damping time constant, and the oscillation frequency, respectively. By averaging the results obtained at several probe wavelengths and for a number of different positions on the sample (see Supporting Information), we obtain $\nu^{[poly]} = 600 \pm 8$ GHz and $\nu^{[single]} = 586 \pm 10$ GHz for the polycrystalline and single crystalline samples, respectively. These frequencies are of the same order of magnitude than the ratio of the sound velocity to the dimension of the studied Co NCs. So, it makes sense to assign the observed oscillations to the modulation of the signal by acoustic vibrations confined in the nanocrystals. For both the polycrystalline and single crystalline NCs we observe a damping time of $\tau_d = 2.82 \pm 0.02$ ps, which is significantly shorter than the inhomogeneous damping time due to the particle size distribution (with size standard deviation $\sigma_R = 0.73$ nm) which can be estimated as $T_2^* = 3.75$ ps.[23,24]

To ascertain such assignment and allow for the proper identification of the vibrational modes observed through our pump−probe measurements, it is interesting to compare the measured frequencies with those calculated using the RUS method, as reported in ref 16. This approach advantageously allows accounting for the elastic anisotropy of the material of which the simulated objects are composed.[25] Also, to simulate polycrystalline Co NCs, an isotropic approximation of cobalt is used, meaning that three-dimensional averaged sound velocities are considered in the RUS calculation. In practice, the longitudinal and transverse sound velocities used to simulate such "virtual" directionally averaged isotropic cobalt material were $\langle v_l \rangle = 5892.8$ m/s and $\langle v_t \rangle = 3087.8$ m/s, respectively. Although the polycrystalline Co NCs are actually not expected to individually vibrate as isotropic spheres, random fluctuations in both the number and position of twinning defects in one particular nanocrystal as compared to the others make it useful to use the isotropic approximation for describing the vibrations of their overall population. On the basis of these considerations, one can assume the frequency of the fundamental radial (breathing) mode of 7.3 nm Co NCs with either polycrystalline or single crystalline structure as being those calculated for Co nanospheres having isotropic and anisotropic elasticity (hexagonal crystallinity), that is, $\nu^{[poly]} = \nu^{[iso]} = 692$ GHz and $\nu^{[single]} = \nu^{[ani]} = 682$ GHz, respectively. These two frequencies are found to be very close from one to the other, thus confirming the experimental observation of the low sensitivity of the breathing mode frequency in Co NCs upon change in their crystallinity. Nevertheless, the theoretical frequencies overestimate by nearly 15% the value obtained from our measurements. The mismatch between the measured and calculated frequencies cannot be attributed to oxidation of Co NCs

because no peak is observed at 8 K in the ZFC curves plotted in Figure 2. It should also be noted that further analyses performed by using various characterization techniques (HRTEM, EELS) did not detect any cobalt oxide.[26] Furthermore, the reasonable reproducibility of the frequency measurements from one sample to the other, whether annealed or not, allows discarding the occurrence of any partial and uncontrolled oxidation of the samples as this latter would randomly affect the vibrational frequency of Co NCs. One possible contribution to the discrepancy between theory and calculations is related to the fact that, as observed in previous studies,[27] the experiments are biased toward larger particles (having lower vibrational frequencies) since the absorption cross sections for metal nanoparticles are proportional to their volume. This effect is not observed in measurements on individual nanoparticles.[28] Nevertheless, note that no such effect was observed in previous Raman studies of a collection of Au nanocrystals with size dispersion as low as 5% (refs 14 and 15). As the size dispersion of the Co NCs under investigation does not exceed 10%, the deviation observed here between the measured and calculated frequencies is not expected to solely result from the bias of the measurements toward the larger particles. Additionally, the calculations were performed on bare NCs, while in the experiments they are capped with dodecanoic acid ligand molecules; this mass loading effect could slightly reduce the acoustic mode frequencies, as already observed in small metal nanoclusters.[29,30] Another effect that could potentially lower the measured vibrational frequencies of Co NCs is related to their mechanical interactions arising from their close packed arrangement in supracrystals. Indeed, such coupling between NCs is likely to disturb their individual vibrations, making the model of a "free" elastic sphere unreliable to accurately predict the vibrational frequencies of the nanocrystals. Moreover, the mismatch between the measured and calculated frequencies could be even more pronounced due to the use of bulk elastic constants in this model, as these constants are probably different from that of the material confined at the nanoscale. The change in the physical parameters of metal (Young's modulus, dielectric constant, stiffness, etc.) resulting from such confinement compared to the bulk ones remains an open question.[12,31−33] It should however be noted that the slight decrease by ~1.5% of the breathing mode frequency predicted using RUS calculation from polycrystalline to single crystalline Co NCs well agrees with the experimentally observed decrease, which is found to be ~2.3%. This result provides therefore additional support to interpret the slight change in breathing mode frequency between polycrystalline and single crystalline Co NCs as being due to the influence of crystallinity on their vibrational dynamics.

CONCLUSIONS

Using a chemical route in reverse micelles to synthesize Co NCs, it is shown that these latter preferentially exhibit a polycrystalline structure in their native state, whereas after annealing at 350 °C, a large amount of these nanocrystals are observed by TEM to be single crystalline with hcp structure. This drastic change in crystallinity is further confirmed by measurement and comparison of their zero-field cooled magnetization *versus* temperature curves.

Measurement of the transient reflectivity signal on both types of nanocrystals allows for the time-domain observation of their fundamental acoustic breathing modes and the quantitative assessment of the related vibration frequencies. The analysis and comparison of the time-resolved responses in polycrystalline and single crystalline Co NCs reveal that no significant effect on the breathing mode frequencies of these nanocrystals occurs upon change in their nanocrystallinity. The low sensitivity of the breathing mode frequency observed in the time-resolved experiments on the nanocrystallinity of the particles is moreover in good agreement with numerical calculations based on the RUS method.

EXPERIMENTAL METHODS

Products. All materials were used without further purification. Cobalt acetate and dodecanoic acid are from Aldrich; isooctane, hexane, and sodium di(ethylhexyl) sulfosuccinate (Na(AOT)) are from Fluka; sodium borohydride is from Acros. The synthesis of cobalt(II) bis(2-ethylhexyl)sulfosuccinate, (Co(AOT)$_2$) has been described previously.[34]

Synthesis of Cobalt NCs. The synthesis of the Co NCs was performed as described in ref 18. The synthesis takes place in pure reverse micelles of Co(AOT)$_2$, whose size and form are controlled by the water content, which is defined here as $w = [H_2O]/[AOT] = 32$. The cobalt ions are reduced by the addition of sodium borohydride, NaBH$_4$, to the micellar solution; the optimal concentration of reducing agent to reduce the size dispersion of the NCs is $R = [NaBH_4]/[Co(AOT)_2] = 6$. After synthesis, the Co NCs are extracted from the AOT surfactant by adding dodecanoic acid molecules that chemically bond to the metallic surface. After being washed several times with ethanol the particles are dispersed in hexane. The solution is then centrifuged to precipitate the largest NC sizes and we recover only the smaller NCs characterized by low size dispersion. The entire synthesis is carried out in a nitrogen glovebox using deoxygenated solvents to prevent particle oxidation.

Sample Preparation and Annealing Process. The 2D superlattices are prepared by depositing a few drops of a colloidal solution (10^{-2} M) on highly ordered pyrolytic graphite (HOPG) grid for TEM analysis. To prepare the HOPG grids, a sheet of HOPG is stuck on an untreated copper grid. The HOPG is then cleaved to give a very thin layer, permitting TEM observations. To prepare the 3D superlattices, HOPG substrates (10 mm × 5 mm) are horizontally immersed in 200 μL of the colloidal NC solution. The solvent evaporation takes place at 25 °C under a nitrogen flow. After deposition, the 2D and 3D superlattices are placed in a closed quartz ampule with a nitrogen atmosphere and are annealed in a furnace at 350 °C for 15 min and subsequently cooled to room temperature in a nitrogen glovebox.

Transmission Electron Microscopy (TEM) and Electron Diffraction (ED). TEM and ED analyses were performed using a Jeol JEM-1011 microscope at 100 kV. High-resolution transmission electron microscopy (HRTEM) was performed using a Jeol JEM-2010 microscope at 200 kV. For these analyses, the nanocrystals are deposited on an amorphous carbon grid.

Magnetic Measurements. Magnetic measurements were carried out using a Cryogenics Ltd. S600 SQUID magnetometer. Zero-field cooled (ZFC) magnetization *versus* temperature measurements were carried out by cooling the sample from 300 to 5 K in zero field then applying a field of 20 Oe and measuring the magnetization while the sample was heated from 5 to 300 K. Field-cooled (FC) measurements were performed in the same manner with the difference that the field was applied before cooling. Magnetization *versus* field measurements were performed at 5 K after zero-field cooling. All magnetic measurements were carried out with the field applied parallel to the substrate.

Time-Resolved Pump—Probe Spectroscopy. The experimental set-up used for the pump—probe studies has been described elsewhere.[35] It is based on a regeneratively amplified Ti:sapphire laser (Clark-MXR, model CPA-1) producing 150-fs, 500-μJ pulses at 800 nm wavelength and 1-kHz repetition rate. A portion of this beam (the pump, with energy up to 5 μJ) is loosely focused on the sample. Another fraction of the pulse is focused in a 2-mm-thick sapphire plate to generate a broadband single-filament white-light continuum (WLC) that acts as a probe after passing through a delay line. The visible portion of the WLC, extending from 430 to 760 nm, is overlapped with the pump beam on the sample. The transmitted/reflected light is dispersed on an optical multichannel analyzer (OMA) equipped with fast electronics, allowing single-shot recording of the probe spectrum at the full 1 kHz repetition rate. By changing the pump—probe delay τ we record 2D maps of the differential transmission ($\Delta T/T$) or reflectivity ($\Delta R/R$) signal as a function of probe wavelength and delay. Our setup achieves, for each probe wavelength, sensitivity down to ~10^{-5}. In this work, Co NCs are deposited on HOPG substrates and are studied in reflection.

Supporting Information Available: Statistical study of the acoustic breathing mode frequencies in single and polycrystalline Co NCs. This material is available free of charge *via* the Internet at http://pubs.acs.org.

REFERENCES AND NOTES

1. Mariotto, G.; Montagna, M.; Viliani, G.; Duval, E.; Lefrant, S.; Rzepka, E.; Mai, C. Low-Energy Raman-Scattering from Silver Particles in Alkali—Halides. *Europhys. Lett.* **1988**, *6*, 239–243.

2. Fujii, M.; Nagareda, T.; Hayashi, S.; Yamamoto, K. Low-Frequency Raman-Scattering from Small Silver Particles Embedded in SiO$_2$ Thin-Films. *Phys. Rev. B* **1991**, *44*, 6243–6248.

3. Palpant, B.; Portales, H.; Saviot, L.; Lerme, J.; Prevel, B.; Pellarin, M.; Duval, E.; Perez, A.; Broyer, M. Quadrupolar Vibrational Mode of Silver Clusters from Plasmon-Assisted Raman Scattering. *Phys. Rev. B* **1999**, *60*, 17107–17111.

4. Hodak, J. H.; Martini, I.; Hartland, G. V. Observation of Acoustic Quantum Beats in Nanometer-Sized Au Particles. *J. Chem. Phys.* **1998**, *108*, 9210–9213.

5. Del Fatti, N.; Voisin, C.; Chevy, F.; Vallee, F.; Flytzanis, C. Coherent Acoustic Mode Oscillation and Damping in Silver Nanoparticles. *J. Chem. Phys.* **1999**, *110*, 11484–11487.

ARTICLE

6. Nisoli, M.; De Silvestri, S.; Cavalleri, A.; Malvezzi, A. M.; Stella, A.; Lanzani, G.; Cheyssac, P.; Kofman, R. Coherent Acoustic Oscillations in Metallic Nanoparticles Generated with Femtosecond Optical Pulses. *Phys. Rev. B* **1997**, *55*, R13424.

7. Nelet, A.; Crut, A.; Arbouet, A.; Del Fatti, N.; Vallee, F.; Portales, H.; Saviot, L.; Duval, E. Acoustic Vibrations of Metal Nanoparticles: High Order Radial Mode Detection. *Appl. Surf. Sci.* **2004**, *226*, 209–215.

8. Duval, E. Far-infrared and Raman Vibrational Transitions of a Solid Sphere: Selection Rules. *Phys. Rev. B* **1992**, *46*, 5795–5797.

9. Portales, H.; Saviot, L.; Duval, E.; Fujii, M.; Hayashi, S.; Del Fatti, N.; Vallee, F. Resonant Raman Scattering by Breathing Modes of Metal Nanoparticles. *J. Chem. Phys.* **2001**, *115*, 3444–3447.

10. Courty, A.; Lisiecki, I.; Pileni, M. P. Vibration of Self-Organized Silver Nanocrystals. *J. Chem. Phys.* **2002**, *116*, 8074–8078.

11. Lamb, H. On the Vibrations of an Elastic Sphere. *Proc. London Math. Soc.* **1882**, *13*, 189–212.

12. Tang, Y.; Ouyang, M. Tailoring Properties and Functionalities of Metal Nanoparticles through Crystallinity Engineering. *Nat. Mater.* **2007**, *6*, 754–759.

13. Stephanidis, B.; Adichtchev, S.; Etienne, S.; Migot, S.; Duval, E.; Mermet, A. Vibrations of Nanoparticles: From Nanospheres to fcc Cuboctahedra. *Phys. Rev. B* **2007**, *76*, 121404.

14. Portales, H.; Goubet, N.; Saviot, L.; Adichtchev, S.; Murray, D. B.; Mermet, A.; Duval, E.; Pileni, M. P. Probing Atomic Ordering and Multiple Twinning in Metal Nanocrystals through Their Vibrations. *Proc. Natl. Acad. Sci. U.S.A.* **2008**, *105*, 14784–14789.

15. Portales, H.; Goubet, N.; Saviot, L.; Yang, P.; Sirotkin, S.; Duval, E.; Mermet, A.; Pileni, M. P. Crystallinity Dependence of the Plasmon Resonant Raman Scattering by Anisotropic Gold Nanocrystals. *ACS Nano* **2010**, *4*, 3489–3497.

16. Saviot, L.; Murray, D. B. Acoustic Vibrations of Anisotropic Nanoparticles. *Phys. Rev. B* **2009**, *79*, 214101.

17. Crut, A.; Maioli, P.; Del Fatti, N.; Vallee, F. Anisotropy Effects on the Time-Resolved Spectroscopy of the Acoustic Vibrations of Nano-objects. *Phys. Chem. Chem. Phys.* **2009**, *11*, 5882–5888.

18. Lisiecki, I.; Pileni, M. P. Synthesis of Well-Defined and Low Size Distribution Cobalt Nanocrystals: The Limited Influence of Reverse Micelles. *Langmuir* **2003**, *19*, 9486–9489.

19. Parker, D.; Lisiecki, I.; Salzemann, C.; Pileni, M. P. Emergence of New Collective Properties of Cobalt Nanocrystals Ordered in fcc Supracrystals: II, Magnetic Investigation. *J. Phys. Chem. C* **2007**, *111*, 12632–12638.

20. Lisiecki, I.; Salzemann, C.; Parker, D.; Albouy, P. A.; Pileni, M. P. Emergence of New Collective Properties of Cobalt Nanocrystals Ordered in fcc Supracrystals: I, Structural Investigation. *J. Phys. Chem. C* **2007**, *111*, 12625–12631.

21. Bao, Y.; Beerman, M.; Pakhomov, A. B.; Krishnan, K. M. Controlled Crystalline Structure and Surface Stability of Cobalt Nanocrystals. *J. Phys. Chem. B* **2005**, *109*, 7220–7222.

22. Voisin, C.; Del Fatti, N.; Christofilos, D.; Vallee, F. Ultrafast Electron Dynamics and Optical Nonlinearities in Metal Nanoparticles. *J. Phys. Chem. B* **2001**, *105*, 2264–2280.

23. Pelton, M.; Sader, J. E.; Burgin, J.; Liu, M.; Guyot-Sionnest, P.; Gosztola, D. Damping of Acoustic Vibrations in Gold Nanoparticles. *Nat. Nanotechnol.* **2009**, *4*, 492–495.

24. Hartland, G. V. Coherent Vibrational Motion in Metal Particles: Determination of the Vibrational Amplitude and Excitation Mechanism. *J. Chem. Phys.* **2002**, *116*, 8048–8055.

25. Visscher, W. M.; Migliori, A.; Bell, T. M.; Reinert, R. A. On the Normal-Modes of Free-Vibration of Inhomogeneous and Anisotropic Elastic Objects. *J. Acoust. Soc. Am.* **1991**, *90*, 2154–2162.

26. Lisiecki, I.; Walls, M.; Parker, D.; Pileni, M. P. 2D Self-Organization of Core/Shell Co_{hcp}/Co Nanocrystals. *Langmuir* **2008**, *24*, 4295–4299.

27. Petrova, H.; Perez-Juste, J.; Zhang, Z.; Zhang, J.; Koselc, T.; Hartland, G. V. Crystal Structure Dependence of the Elastic Constants of Gold Nanorods. *J. Mater. Chem.* **2006**, *16*, 3957–3963.

28. Zijlstra, P.; Tchebotareva, A. L.; Chon, J. W. M.; Gu, M.; Orrit, M. Acoustic Oscillations and Elastic Moduli of Single Gold Nanorods. *Nano Lett.* **2008**, *8*, 3493–3497.

29. Miller, S. A.; Womick, J. M.; Parker, J. F.; Murray, R. W.; Moran, A. M. Femtosecond Relaxation Dynamics of $Au_{25}L_{18}^-$ Monolayer-Protected Clusters. *J Phys. Chem. C.* **2009**, *113*, 9440–9444.

30. Qian, H.; Sfeir, M. Y.; Jin, R. Ultrafast Relaxation Dynamics of $[Au_{25}(SR)_{18}]^q$ Nanoclusters: Effects of Charge State. *J. Phys. Chem. C* **2010**, *114*, 19935–19940.

31. Scaffardi, L. B.; Tocho, J. O. Size Dependence of Refractive Index of Gold Nanoparticles. *Nanotechnology* **2006**, *17*, 1309–1315.

32. Gu, Q. F.; Krauss, G.; Steurer, W.; Gramm, F.; Cervellino, A. Unexpected High Stiffness of Ag and Au Nanoparticles. *Phys. Rev. Lett.* **2008**, *100*, 045502.

33. Juvé, V.; Crut, A.; Maioli, P.; Pellarin, M.; Broyer, M.; Del Fatti, N.; Vallée, F. Probing Elasticity at the Nanoscale: Terahertz Acoustic Vibration of Small Metal Nanoparticles. *Nano Lett.* **2010**, *10*, 1853–1858.

34. Petit, C.; Lixon, P.; Pileni, M. P. *In-Situ* Synthesis of Silver Nanocluster in AOT Reverse Micelles. *J. Phys. Chem.* **1993**, *97*, 12974–12983.

35. Polli, D.; Luer, L.; Cerullo, G. High-Time-Resolution Pump–Probe System with Broadband Detection for the Study of Time-Domain Vibrational Dynamics. *Rev. Sci. Instrum.* **2007**, *78*, 103108.